GaS:WS_2 Heterojunctions for Ultrathin Two-Dimensional Photodetectors with Large Linear Dynamic Range across Broad-Wavelengths

Yang Lu,[1] Tongxin Chen,[1] Nhlakanipho Mkhize,[1] Ren-Jie Chang,[1] Yuewen Sheng,[1] Philip Holdway,[1] Harish Bhaskaran,[1] Jamie H. Warner[2,3]*

[1]Department of Materials, University of Oxford, Parks Road, Oxford, OX1 3PH, United Kingdom

[2]Walker Department of Mechanical Engineering, The University of Texas at Austin, 204 East Dean Keeton Street, Austin, Texas, 78712, United States

[3]Materials Graduate Program, Texas Materials Institute, The University of Texas at Austin, 204 East Dean Keeton Street, Austin, Texas, 78712, United States

*email: Jamie.warner@austin.utexas.edu;

Abstract:

2D photodetectors based on photovoltaic effect or photogating effect can hardly achieve both high photoresponsivity and large linear dynamic range at the same time, which greatly limits many practical applications such as imaging sensors. Here, conductive sensitizer strategy, a general design for improving photoresponsivity and linear dynamic range in 2D photodetectors is provided and experimentally demonstrated on vertically stacked bilayer $WS_2/GaS_{0.87}$ under a parallel circuit mode. Owing to successful band alignment engineering, the isotype type-II heterojunction enables efficient charge carrier transfer from WS_2, the high-mobility sensitizer, to $GaS_{0.87}$, the low-mobility channel, under illumination from broad visible spectrum. The transferred electron charges

introduce a reverse electric field which efficiently lowers the band offset between the two materials, facilitating a transition from low-mobility photocarrier transport to high-mobility photocarrier transport with increasing illumination power. A large linear dynamic range of 73 dB as well as a high and constant photoresponsivity of 13 A/W under green light is achieved. X-ray photoelectron spectroscopy, cathodoluminescence and Kelvin probe force microscope further identify the key role of defects in monolayer $GaS_{0.87}$ in engineering the band alignment with monolayer WS_2. This work proposes a design route based on band and interface modulation for improving performance of 2D photodetectors, and provides deep insights into the important role of strong interlayer coupling in offering heterostructures with desired properties and functions.

keywords: type-II heterojunction, Gallium Sulfide (GaS), Tungsten Disulfide (WS_2), photodetector, linear dynamic range.

Introduction

Photodetectors, where light signals are converted into electrical signals, have vast application implications such as imaging, optical communication, gas sensing and motion detection.[1-2] In recent years, 2D semiconductors have attracted huge enthusiasm in this field. The atomically thin dimension offers them with strong light-matter interactions such as ultrahigh absorption coefficient and large exciton binding energy.[3-4] Their band structure can be facially tuned by various parameters including thickness, strain, dopants and defects.[5-7] With regard to its anisotropic morphology, the van der Waals bonding between layers enables fabrication of vertical heterostructures free of lattice mismatch and dangling bonds problems.[8-12] At the same time, the

strong interlayer coupling behavior such as ultrafast charge separation and moiré excitons further demonstrate its potential to incorporate further functionalities in vertical heterostructures.[13-16]

In practical photodetector applications such as for imaging systems, it is critical to have high and linear photoresponse over a large intensity range of incident light power to convert light signals into accurate electric signals.[17-19] Current 2D photodetectors, however, often find it difficult to satisfy both requirements at the same time. The problem lies in the fundamental photodetection mechanism. Two mechanisms are most commonly used by 2D photodetectors. In photovoltaic effect (PVE), photocurrent is formed by separation of photogenerated electron-hole pairs under built-in fields from junction interfaces.[9, 20] While good linearity is obtained due to stable carrier lifetime, it shows small electric signals in the order of mA/W limited by the absorbance of the ultrathin layer.[21-25] For example, exfoliated few-layer GaSe/MoS_2 *p*-*n* diode show linear response (with linear dynamic range of 70 dB) and comparatively low photoresponsivity of 50 mA/W.[26] Alternatively, in photodetectors based on photogating effect (PGE), photogenerated minority carriers are trapped at localized states, acting as local gate.[20, 27] With a large surface ratio, 2D materials show high sensitivity up to 10^7 A/W under low illumination power.[28] However, the responsivity decays exponentially under higher illumination power primarily due to trap saturation.[29-31] Photogain, which is defined as the number of collected carriers in the photocurrent for every excited electron by incident light, can provide more insights behind the decaying photoresponse. The photogain in PGE can be expressed as:[27]

$$G = \frac{\tau \mu E}{L}$$

where τ is the excess carrier lifetime, μ is the carrier (electron and hole) mobility, E is the electric field provided by bias voltage and L is the channel length. In PGE mechanism, trap states promote

photogain by introducing a long carrier lifetime. Further excitation creates more free carriers due to gradually filled trap states, resulting in decreased average carrier lifetime. While trap states are helpful in promoting sensitivity for low signals, there lack solution to maintain high photogain under increasing illumination.

We present a conductive sensitizer strategy that could tune the photoresponse's power-dependent relations, especially to mitigate or even stop the decaying tendency while preserving the high-sensitivity benefits from trap states. To achieve stable photogain, the decrease in average carrier lifetime must be compensated by increase in average mobility. Such behavior of varying mobility with illumination power has been found in conventional sensitizer-channel hybrid photodetectors. Incorporation of a photosensitive material to tune the absorption behavior of photodetectors has been reported to enhance device performance,[32-33] such as in 0D-2D hybrid PbS-MoS_2 photodetectors.[34] Photocurrent is generated by electrons transferred into MoS_2 channel after being excited in PbS quantum dot sensitizer, in which holes are trapped and the remaining electrons have little direct contribution to conductivity. In these kinds of devices, a similar 10^3-times decrease in photoresponse under higher illumination is attributed mainly to the increasing inverse electric field from growing numbers of transferred charge carriers, which reduces the charge transfer rate. As conventional sensitizers typically have low mobility, the average mobility (which is the linear combination of individual channel mobilities by carrier proportions) for majority carriers in the device reduces when more and more photogenerated new carriers stay in the sensitizer. In contrast, in our conductive sensitizer strategy (Figure 1), the sensitizer is more conductive than the channel, thus a transition to higher-mobility carrier transport at higher illumination power is realized. The device configuration is shown in Figure 1a, where both high-mobility sensitizer and low-mobility channel are connected to the electrodes in parallel. The strategy also demands specific band

alignment engineering (see Figure 1b). The sensitizer (smaller bandgap) and channel (larger bandgap) should form an isotype type-II heterojunction (schematics showing the *n*-*n* case), and the band offset should be large to enable efficient majority carrier transfer from sensitizer to channel as well as channel-dominated transport at the beginning. A transition from low-mobility to high-mobility transport under high illumination power is therefore achieved for photons that only excite the sensitizer: under dark or low illumination power, a large conduction band offset indicates low carrier concentration in the sensitizer conduction band (S-CB), thus at steady regime most photogenerated electrons contribute to photocurrent from the channel conduction band (C-CB) while holes trapped in the sensitizer. Under high illumination power, the increasing reverse electric field from transferred carriers efficiently reduces the band offset and charge transfer rate, thus photocurrent contribution from the high-mobility sensitizer gradually become dominant. Such efficient change in band offset cannot be achieved by back gating or photons that excite both channels. The photogain (and subsequently the photoresponsivity) decay can therefore be mitigated as long as the mobility rise compensates for the carrier lifetime fall.

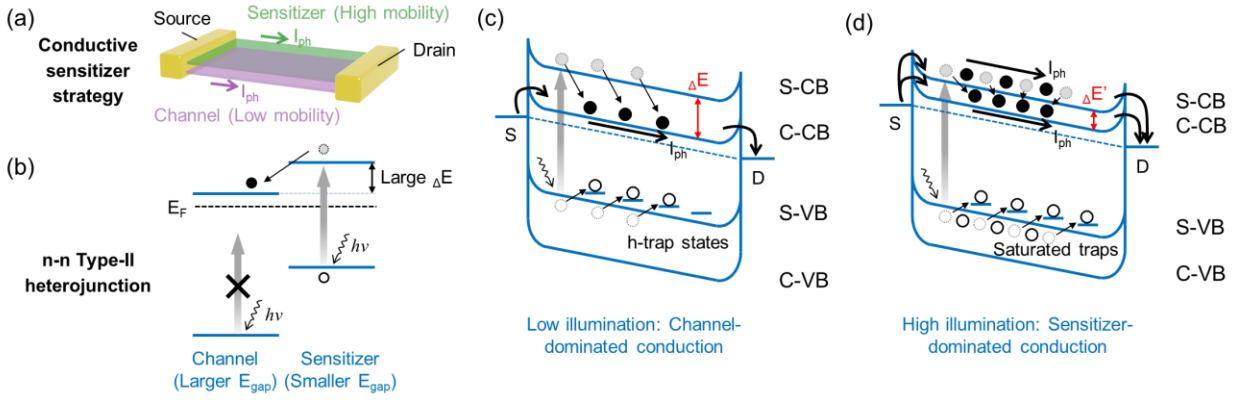

Figure 1. Conductive sensitizer strategy for realizing 2D photodetectors with high sensitivity and linearity response. (a) Device configuration of the proposed 2D photodetector where both channel and sensitizer are in contact with electrodes in parallel. (b) Band alignment engineering of the channel-sensitizer

isotype type-II heterojunction (*n-n* type-II heterojunction is drawn as an example). The sensitizer should have a smaller bandgap so that only the sensitizer generates excitons upon illumination. In addition, the conduction band offset $_{\Delta}E$ between the sensitizer and channel should be large to enable efficient charge transfer and guarantee small carrier concentration in the sensitizer conduction band in dark. (c) Band schematic of device under weak light irradiation. The sensitizer absorbs light, generates excitons, and electrons are transferred into the channel conduction band (C−CB) while holes are trapped in trap states, a photogating effect known to promote sensitivity. Due to large $_{\Delta}E$, the sensitizer conduction band (S−CB) with small carrier concentration contributes little to the photocurrent, which is dominated by the low-mobility channel. (d) Band schematic of device under intense light irradiation. Carrier lifetime in both sensitizer and channel decrease due to trap saturation. At the same time, the increasing inverse electric field from transferred carriers results in a smaller $_{\Delta}E'$, leading to increasing participation in photocurrent from the high-mobility sensitizer. This shift to high-mobility-sensitizer-dominated conduction slows the decreasing trend in photogain from saturated trap states.

To demonstrate this conductive sensitizer strategy, we fabricate 2D bilayer $WS_2/GaS_{0.87}$ photodetectors accordingly which achieve both high sensitivity and large linear range. We select WS_2 with high absorbance as sensitizer and non-stoichiometric $GaS_{0.87}$ with wide bandgap as channel which could form the isotype type-II heterojunction.[35-37] The defective $GaS_{0.87}$ has been reported as an ambient-stable phase with many intrinsic defects that lead to low mobility.[38] The band alignment was examined to match the conductive sensitizer strategy using combined technique of X-ray photoelectron spectroscopy (XPS), cathodoluminescence (CL) and photoluminescence (PL) spectroscopy. Efficient charge carrier transfer from WS_2 to $GaS_{0.87}$ was probed by Kelvin probe force microscope (KPFM) and Raman, PL spectroscopy. Finally, electronic and optoelectronic characterizations confirmed the transition from $GaS_{0.87}$ dominated

low-mobility transport to WS_2 dominated high-mobility transport behavior predicted by the conductive sensitizer strategy. With wide bandgap in the visible spectrum and a large bandgap difference, for photons from red to blue (470−622 nm), bilayer $WS_2/GaS_{0.87}$ heterostructure photodetectors successfully demonstrated stable photoresponsivity with illumination power, and achieved both large linear dynamic range of 73 dB and high photoresponsivity of 13 A/W under green light.

Results and discussions

Figure 2a shows the atomic structure of the $WS_2/GaS_{0.87}$ heterostructure, which is stacked according to the schematic diagrams in Figure 2b: First, monolayer $GaS_{0.87}$ and WS_2 crystals are synthesized by chemical vapor deposition (CVD) on 300 nm SiO_2/Si substrates *via* methods developed in previous reports.[38-39] Compared with mechanical exfoliation, the CVD-grown materials facilitate facile tuning of defects as well as fabrication of large-scale devices.[40] The synthesized monolayer WS_2 domains show triangular shape with an edge length of ~100 μm, while monolayer $GaS_{0.87}$ has morphology in continuous monolayer films or round-corner triangular shaped domains with an edge length of ~35 μm (see Fig. S1a-c for additional optical and SEM images). The consistent stoichiometries of $GaS_{0.87}$ were identified in detail in our previous report according to XPS and EDX characterizations.[38] Then, the WS_2 crystals are transferred onto the $GaS_{0.87}$ crystals by a wet-transfer method (see Methods). The fabricated structure is further annealed in sulfur environment at 200 °C for better interlayer interactions. After transfer and annealing, we characterized the Raman or PL of individual $GaS_{0.87}$ and WS_2, and found no sign of material degradation. Most importantly, $GaS_{0.87}$ did not turn into stoichiometric GaS after sulfur annealing. The individual and heterostructure regions could be clearly distinguished under optical

microscopy but obscure under SEM due to the very small height contrast (see Figure 1c and Figure S1d). AFM height scan provides accurate information on sample thickness. As shown in Figure S2a-b, the $GaS_{0.87}$ crystals show a height of 0.85 nm and the WS_2 layer on top is 0.75 nm in thickness, which are in accordance with previous reports and indicate that polymer residues could be ignored.[41-42]

The band alignment of the $WS_2/GaS_{0.87}$ heterostructure is then determined with band offset and bandgap information. First, the valence band offset (VBO) is obtained using the core levels energy and the valence band maximum extracted from XPS results. According the Kraut's method, the VBO of WS_2 and $GaS_{0.87}$ could be determined using the following equation:[43]

$$VBO = (E_{W4f7/2} - VBM)_{WS2} - (E_{Ga3d} - VBM)_{GaS} - (E_{W4f7/2} - E_{Ga3d})_{WS2/GaS}$$

As shown in Figure 2d, the VBO of $WS_2/GaS_{0.87}$ is calculated as 32.01−19.16−11.93=0.92 eV. The uncertainty in determining peak positions is 0.03 eV and for fitting VBM position is 0.07 eV. Note that the measured region in our heterojunction sample is continuous monolayer $GaS_{0.87}$ film covered with some isolated WS_2 domains (see Fig. S3 for optical images). Therefore, Ga signals from two origins would co-exist: one corresponding to uncovered $GaS_{0.87}$ and the other arising from the heterojunction (noted as Ga*). They were separated during curve fitting according to W:Ga atom ratio (the ratio x is derived from relative signal from XPS, which gives Ga*:Ga_{total} ratio as $2x/(1-2x)$ given the monolayer thickness). Then, bandgap of each material is measured. Bandgap of WS_2 is determined as 2.00 eV from PL spectrum (see PL analysis section). Monolayer $GaS_{0.87}$ shows no signal under the 532 nm laser due to a large bandgap, thus cathodoluminescence (CL) spectroscopy is used where electrons are excited across the gap by electron beam in SEM. Fitting of $GaS_{0.87}$ CL spectrum in Figure 2e shows two emission peaks. The high energy emission at 3.35 eV is also found in CL spectrum of stoichiometric GaS (see Figure S4b), which has been

reported previously for recombination from monolayer GaS conduction band.[35] The other one at 2.73 eV is attributed to a new defect-induced band (DB). The resulted band alignment schematic is drawn in Figure 2f. As the defect-induced band in $GaS_{0.87}$ is 0.19 eV lower than the conduction band minimum of WS_2, a *n-n* isotype type-II heterojunction is formed. The defect-induced band is key to achieving the type-II heterojunction and the channel's low mobility required by the conductive sensitizer strategy. Without that, the conduction band of stoichiometric GaS is determined to be 0.77 eV higher than that of WS_2 in the as-formed heterostructure (CBO=VBO+2.00−3.35=−0.77 eV, see Figure S4a-b), suggesting formation of a type-I heterojunction (Figure S4c).

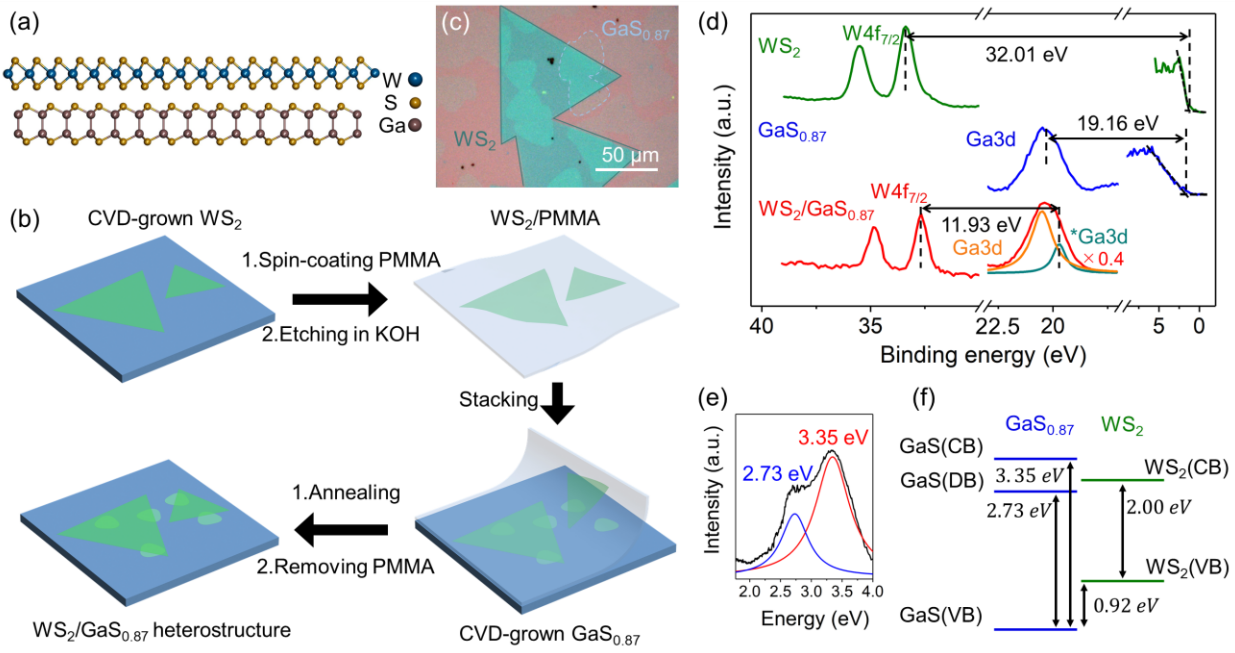

Figure 2. Fabrication and band alignment of $WS_2/GaS_{0.87}$ heterostructure. (a) Atomic structure of bilayer $WS_2/GaS_{0.87}$ heterostructure. (b) Schematic illustration for fabrication of bilayer $WS_2/GaS_{0.87}$ heterostructure. (c) Optical image of fabricated WS_2/GaS heterostructure. (d) XPS of WS_2, $GaS_{0.87}$ and $WS_2/GaS_{0.87}$ samples for calculating VBO from Kraut's method; (e) CL of monolayer $GaS_{0.87}$ sample; (f) Schematic of $WS_2/GaS_{0.87}$ band alignment reconstructed from XPS and CL analysis.

Next, we confirm charge carrier transfer from WS_2 conduction band to $GaS_{0.87}$ defect-induced band. KPFM mapping was used to determine the work function and band bending of the type-II heterojunction (see Figure 3a).[5] Figure 3b shows the contact potential differences (CPD) across the orange line in Figure 3a (also see Fig. S5) which contains all three different surfaces: WS_2, $GaS_{0.87}$, and $WS_2/GaS_{0.87}$ (W/G). The CPD is related to the work function (Φ) difference between the material and tip surface by $\Phi_{sample} = \Phi_{tip} - e*CPD$. Therefore, the difference between the work function of WS_2 on top of $GaS_{0.87}$ or the substrate is obtained as $\Phi_{W/G} - \Phi_{WS2} = 0.04$ eV, and that between the work function of $GaS_{0.87}$ and WS_2 is obtained as $\Phi_{W/G} - \Phi_{GaS0.87} = -0.10$ eV. Since the Fermi level at the junction in equilibrium is constant, the energy levels of WS_2 bend 0.04 eV upwards at the junction, and the energy levels of $GaS_{0.87}$ bend 0.10 eV downwards at the junction, as shown in Figure 3c. The observation suggests that electrons are transferred from WS_2 to $GaS_{0.87}$ at the atomical sharp interface upon heterojunction formation.

To further understand charge transfer behavior between the two semiconductors under illumination, Raman and PL spectroscopy with 532 nm laser excitation source were used to probe the interlayer coupling. In all analysis, the measurement conditions were kept the same so that signal intensities can be directly compared. Raman and PL spectra of the individual components were found to be consistent with previous reports, suggesting a good quality in the material we used. The A^1_{1g} peak signal of $GaS_{0.87}$ corresponds to out-of-plane vibration mode, whose position has been reported as an indicator of layer of numbers.[38, 42] Raman spectrum of monolayer defective $GaS_{0.87}$ shows A^1_{1g} peak at 182.6 cm^{-1} (Fig. 3d). As the 532 nm (2.33 eV) photon energy is smaller than the bandgap of $GaS_{0.87}$, PL signal was not observed (Fig. 3g). Fitting of Raman spectrum of pristine WS_2 shows E_{1g} peak at 356.1 cm^{-1} and A_{1g} peak at 416.4 cm^{-1} (Fig. 3e), while PL spectrum shows exciton

peak (A) at 2.003 eV, trion peak (A^-) at 1.980 eV, and a small but broad localized state (LS) peak at ~1.9 eV, indicating the inevitable presence of certain structural disorder or impurities introduced during the transfer process (Fig. 3h).[44-45] The exciton-to-trion ratio (I_A/I_{A^-}) is determined to be 0.43±0.03 in WS_2 on SiO_2/Si substrate, due to *n*-type doping introduced by SiO_2 interface or polymer/solvent residues. Additional discussions on using three-Lorentzian peak fitting were provided in Figure S7.

Since Raman and PL signals from $GaS_{0.87}$ are very small (<1%) compared with WS_2, the signals from heterostructure are regarded as generated by WS_2, therefore they are compared with monolayer WS_2 and show changes in various peak positions and intensities after forming the heterostructure. Previous studies have shown that the signals can be affected by many factors including strain effect, trap states from environment, free charge carriers, environmental dielectric screening effect, *etc*.[46-49] We first exclude impacts from trap states by molecular physisorption as the transfer process should bring the same impact on WS_2 on SiO_2 or on $GaS_{0.87}$. The E_{1g} peak position of WS_2 could be used to probe the level of strain presented in the crystal.[50-51] As WS_2 in heterostructure shows little variation (< 0.2 cm^{-1}) in E_{1g} peak position, strain effects are also ruled out (Figure 3f). A lower carrier density in WS_2 in the heterostructure is supported by a blue-shift of A_{1g} peak position in $WS_2/GaS_{0.87}$ from 416.4 cm^{-1} to 417.4 cm^{-1} as well as an increasing I_A/I_{A^-} in PL from 0.43 to 1.42.[50] The free electron carrier concentration in the WS_2 layer can be calculated from the I_A/I_{A^-} ratio with the following relation:[50]

$$\frac{I_{A^-}}{I_A} = \frac{\gamma_{A^-}}{\gamma_A}\left(\frac{\pi\hbar^2 m_{A^-}}{4m_A m_e}\right)\frac{n_e}{k_B T}\mathrm{e}^{\frac{E_{trion}}{k_B T}}$$

where γ is the radiative decay rate of exciton and trion (assuming γ is constant in the doping level range and γ_{A^-}=0.02 ps^{-1}, γ_A=0.002 ps^{-1}); m_A and m_{A^-} is the effective mass of exciton and trion

($m_A=m_e+m_h$, and $m_{A^-}=2m_e+m_h$; in monolayer WS_2 $m_e=0.44m_0$, and $m_h=0.45m_0$); and E_{trion} is the trion binding energy. The results (see Table 1) show that carrier densities of WS_2 in $WS_2/GaS_{0.87}$ heterostructure ($1.6*10^{13}$ cm^{-2}) is only 25% compared with that in pristine WS_2 ($6.2*10^{13}$ cm^{-2}). Such reduction in free electron carrier concentration is attributed to both reduced *n*-type doping and charge transfer. Reduction of *n*-type doping from SiO_2 interface is commonly observed for WS_2 stacked on another 2D substrates.[52] However, decreased doping level alone would result in higher PL intensity as quantum efficiency is greatly increased, which is against an observed 52% quenching in total PL intensity.[53] Quenching in heterostructure can originate from two principal mechanisms: energy transfer or charge transfer. However, energy transfer quenching must occur from a high energy transition to a low energy transition, which is impossible here for the smaller bandgap of WS_2.[54] Thus, electron carrier transfer from WS_2 to $GaS_{0.87}$ under light illumination is confirmed. After the electron in WS_2 is excited to its conduction band, instead of forming intralayer bounded exciton, the electron could undergo ultrafast transfer at the 2D interfaces into the $GaS_{0.87}$ lower band, leading to the formation of interlayer bounded exciton.[13] The interlayer exciton is suspected to be indirect as no extra PL peak was observed.

In addition to quenching of PL intensity and increase in I_A/I_{A^-}, we also note the changes in A peak position for the type-II heterostructure by a red shift of ~22 meV, due to the combined effects from varied quasiparticle bandgap and exciton binding energy which are attributed to the screening effects from both free charge carrier and dielectric environment.[55-56] The above parameters obtained from spectral fittings are summarized in Table 1. For additional comparison, spectral data from type-I heterojunction of WS_2/GaS(stoichiometric) without charge transfer also support the above analysis and exclude the exciton-exciton annihilation effect in our measurements (Figure

S6).[57] Mapping results are also provided to present clear distinction between pristine WS_2 and heterostructures regions as well as the spatial uniformity (Figure S8-9).

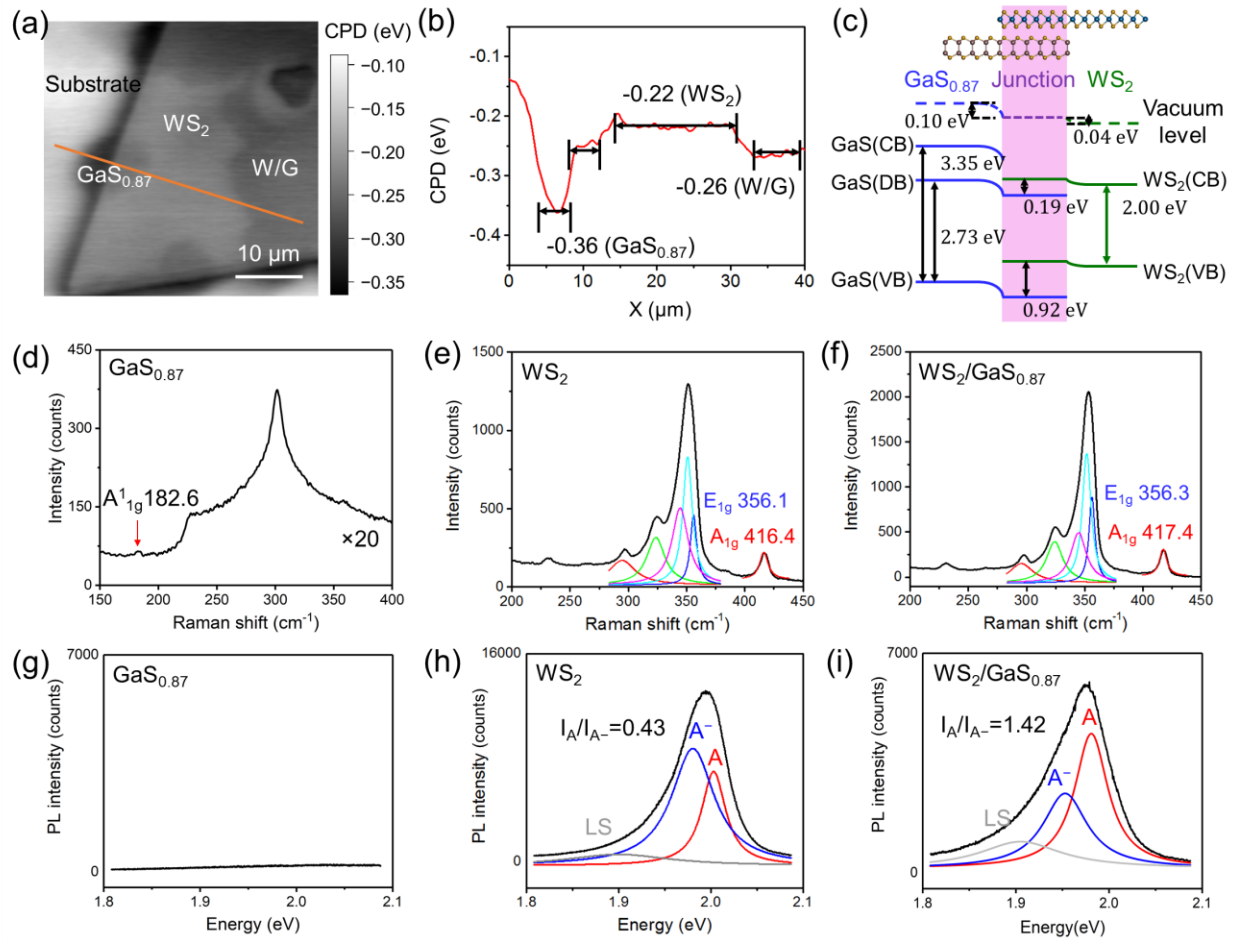

Figure 3. **Charge transfer in $WS_2/GaS_{0.87}$ heterostructures.** (a) KPFM scanning of $WS_2/GaS_{0.87}$ heterostructures. (b) CPD line profile in (a). (c) Schematic of band bending in $WS_2/GaS_{0.87}$ heterostructures in the lateral direction, suggesting charge transfer upon heterojunction formation. (d-f) Raman spectrum of (d) monolayer $GaS_{0.87}$, (e) monolayer WS_2 and (f) $WS_2/GaS_{0.87}$ heterostructure (532 nm, 620 μW). (g-i) PL spectrum of (g) monolayer $GaS_{0.87}$, (h) monolayer WS_2 and (i) $WS_2/GaS_{0.87}$ heterostructure (532 nm, 6 μW). The increasing I_A/I_{A^-} as well as strong quenching effect in the heterostructure suggest electron carrier transfer from WS_2 to $GaS_{0.87}$ and formation of interlayer excitons.

Table 1. Average of extracted parameters from Raman and PL fitting

	$A_{1g}(cm^{-1})$	$E_{1g}(cm^{-1})$	A (eV)	A^- (eV)	PL intensity relative to WS_2	I_A/I_{A-}	n_e in WS_2 (cm^{-2})	E_{trion} (meV)
WS_2	416.4	356.1	2.003±0.002	1.980±0.002	1.00	0.43±0.03	$6.2*10^{13}$	23
$WS_2/GaS_{0.87}$	417.4	356.3	1.981±0.002	1.954±0.002	0.48	1.42±0.006	$1.6*10^{13}$	27

As analyzed above, the heterostructure's band alignment and charge transfer behaviors satisfy the requirements for the conductive sensitizer strategy. Therefore, photodetector devices based on configurations shown in Figure 1a were fabricated by e-beam lithography with gold as electrodes on top of the 2D material. Figure 4c-d shows the schematics and optical images of the Au−$WS_2/GaS_{0.87}$−Au FET device. To demonstrate the heterostructure properties, FET devices based on its individual components, Au−WS_2−Au and Au−$GaS_{0.87}$−Au, were also fabricated and studied as a reference (Figure 4a-b). A $GaS_{0.87}$-dominated conducting mode is suggested by our measurements under dark. Although the value of $GaS_{0.87}$ mobility was difficult to obtain from its low current (possibly due to both a low mobility and the large contact barrier with gold electrode), mobility of WS_2 and $WS_2/GaS_{0.87}$ heterostructure is calculated to be 0.13 $cm^2V^{-1}s^{-1}$ (similar to other CVD-grown WS_2) and 0.0014 $cm^2V^{-1}s^{-1}$, respectively, from transfer curves in Figure 4e-f.[41, 58] This 100-times smaller value in mobility cannot come from WS_2 layer even if screening effect from the bottom $GaS_{0.87}$ are considered, but instead should come from the defective $GaS_{0.87}$ channel. Because mobility is proportional to current density, the heterostructure's mobility is the combination of contribution from both layers. From the measured band offset (ΔE=0.19 eV) we

can estimate the carrier density ratio $n_{GaS0.87}$:n_{WS2}≈exp(ΔE/k_BT)≈1.5*10^3. Thus, the mobility contribution from WS_2 monolayer in dark is less than 0.0001 $cm^2V^{-1}s^{-1}$, and the heterostructure's small mobility mainly comes from the $GaS_{0.87}$ channel. Measurement of effective Schottky barrier also reveals $GaS_{0.87}$ as main transport channel. Metal-2D material junctions are known to form Schottky barrier which is largely determined by defects at the interface.[59] Applying a back-to-back model, the effective Schottky barrier height (Φ_{B_eff}) in the monolayer WS_2 devices is determined as 0.57 eV (0.52 eV under flat-band condition, Fig. S10b-c).[60] For the heterostructure devices, since the gold electrodes are deposited onto the top WS_2 under same conditions, the interface should be the same. Based on the band diagram in Figure 3c, the WS_2 conduction band should be positioned 0.61 eV above the Fermi level owing to the upward band bending, and subsequently the $GaS_{0.87}$ defect-induced band should be positioned 0.42 eV above the Fermi level (see Schematics in Figure 4g-h). Our measured Φ_{B_eff} of WS_2/$GaS_{0.87}$ FET devices is 0.43 eV, very close to the $GaS_{0.87}$ band position. These results further confirm that under dark, the dominant pathway for electron carrier transport is $GaS_{0.87}$.

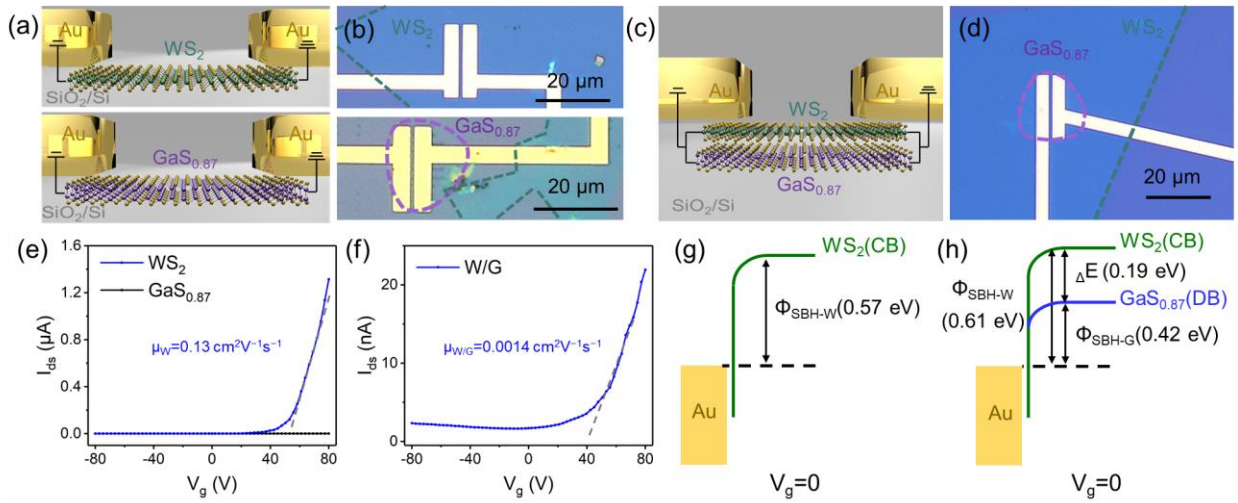

Figure 4. Electronic properties of $GaS_{0.87}$, WS_2 and WS_2/$GaS_{0.87}$ devices. (a) Schematic and (b) optical image of Au−WS_2−Au (Up) and Au−$GaS_{0.87}$−Au (Bottom) FET device. (c) Schematic and (d) optical image

of Au−WS_2/$GaS_{0.87}$−Au FET device. (e) Transfer curves of WS_2 and $GaS_{0.87}$ FET devices (Dark, V_{ds}=2 V). (f) Transfer curve of WS_2/$GaS_{0.87}$ FET device (Dark, V_{ds}=2 V). (g) Schematic of measured Schottky barrier in Au−WS_2−Au FET device. (h) Schematic of estimated Schottky barriers in Au−WS_2/$GaS_{0.87}$−Au FET device.

Finally, the optoelectronic properties of the individual and heterostructure devices were studied. The photoresponse of these devices were measured under various wavelengths (395 nm, 470 nm, 535 nm, 590 nm, 622 nm) across wide power range. As an example, photocurrent−voltage curves of devices under 535 nm were shown in Figure 5a-b. Photoresponsivity ($R_\lambda \equiv I_{photo}/P$) is used to demonstrate the sensitivity of photodetectors to incident light where I_{photo} is the photocurrent and P is the illumination power. When comparing the wavelength-dependent R_λ with the material's absorption spectrum in Figure S11, we found that for WS_2 devices, the R_λ is in accordance with the WS_2 absorption spectrum. In comparison, for the heterostructure devices, the R_λ is in accordance with the WS_2 absorption spectrum for photon energy below 2.73 eV (470 nm, 535 nm, 590 nm, 622 nm), but show unproportionally higher R_λ for 395 nm. This is consistent with the WS_2-sensitized photodetector behavior for photons within 2.00~2.73 eV range, which takes up most of the visible spectrum. Above this energy, carriers in $GaS_{0.87}$ valence band could be excited and contribute to the photocurrent. Such differences indicate that the heterostructure would operate under C(conductive)-Sensitizer mode within 2.00~2.73 eV, but turn to PGE mode for photon energy higher than 2.73 eV.

The power-related change in photocurrent can be characterized by the power dependence parameter α, defined by the relation $I_{photo} \propto P^{\alpha}$. For ideal linear response, the α value should be 1, while a small α value indicates severe photoresponse decay. For monolayer WS_2 devices, R_λ shown

in Figure 5g is in the range of 30−700 A/W under various visible light and power. A smaller α value of 0.5~0.7 was measured for different wavelengths, which is typical for PGE mechanism (see Figure 5c). In addition, both defective and stoichiometric gallium sulfide photodetectors under 275 nm UV light excitation show similar small α values in our previous report.[38] However, the heterostructure devices based on the conductive sensitizer strategy show greatly reduced photoresponse decay and exhibit a nearly ideal α value of 0.97~1.03 for photons between 2.00~2.73 eV, with a moderate photoresponsivity of 10−25 A/W compared to other PGE devices and a detectivity of 1.5×10^9 Jones for red light (see Figure 5d). The significant difference in decaying behavior from individual components implies that it originates from coupling effects. At near-UV spectrum, the photodetector operates under the PGE mechanism, thus leading to 20% decay in photoresponsivity with increasing power from 50 to 164 μW/cm^2, similar to other PGE photodetectors (see Figure 5d).

The $WS_2/GaS_{0.87}$ heterostructure should share some strong characteristics of the trap-based PGE, such as large photogain and long response time, as the sensitizer has trap states. The photogain (calculated by $G=h\nu R_\lambda/e\eta$, where η is the absorbance) is estimated to be in the range of 480−1070 in the visible spectrum range, demonstrating a highly efficient process in absorption, charge transfer and photocarrier transport. A long response time of 5 s is also similar to that of pristine WS_2 photodetectors (12 s) and other PGE photodetectors (see Figure S12).[27, 61] Still, a major difference between PGE or conductive sensitizer strategy is the change in mobility, which is revealed by the transfer curves under illumination. As shown in Figure 5e, transfer curve of the heterostructure under UV light show significant threshold voltage shift but little change in transconductance (defined as $g_m\equiv\partial I_{ds}/\partial V_{OG}$, where V_{OG} is the overdrive gate voltage from the threshold voltage point), which is typical for conventional PGE mechanism where traps act as local

gates.[62] However, transfer curve of the heterostructure under green light with the same illumination power show totally different behaviors, with significant increase in transconductance and little shift in threshold voltage. Such increased transconductance indicates larger mobility that originates from additional contribution from WS_2 sensitizer. Other transfer curves measured under various illumination wavelength and power also exhibit distinct behavior under UV and visible illumination (see Figure S13a-b).

As charge transport is in the parallel mode, the transfer curves under visible illumination show both threshold voltage shift and change in interlayer charge transfer, whose effect can be separated by fitting the ON-state transfer curve (see Supplementary Note for detailed information). This enables quantitively extracting the change in heterojunction's mobility, the threshold voltage and band offsets (see Figure S13c-e). In Figure 5f, the heterojunction's mobility is directly evidenced to increase by a factor of 2 when the visible photon flux (photons absorbed per second, to exclude the influence of photon energy difference on illumination power) increased by a factor of 10, showing increasing participation from the WS_2 layer. In comparison, under UV illumination of similar photon flux, the device exhibits almost unvaried mobility of 0.002 $cm^2V^{-1}s^{-2}$ (GaS-dominated).

Such a difference between the PGE mode and the C(conductive)-sensitizer mode for different photon energy is further illustrated in Figure 5g. Under C-sensitizer mode, light is only absorbed by the sensitizer. The excited electrons then tunnel into the underlying channel, contributing to photocurrent but also creating a reverse electrical field. At higher illumination power, the subsequent electrons have a lower possibility of tunneling and thus a higher possibility to contribute to photocurrent from the high-mobility sensitizer. Under the PGE mode, photons are absorbed both by the sensitizer and the channel. Light absorbed by underlying $GaS_{0.87}$ populates

its own band with electrons, leaving less available states for charge to tunnel from WS_2. Thus, with less transferred electrons, the reverse electrical field is comparably smaller than that in the C-sensitizer mode, and is not enough to hinder the decaying tendency in photoresponse from decreased photocarrier lifetime. It should be noted that for Schottky type contacts, strong illumination power leads to increased electric field in the channel due to lowered Schottky barrier height. However, the increase in electric field alone can hardly compensate for the exponential decayed carrier lifetime in previous reports,[4, 29, 71] thus increase in mobility is essential for further tuning the photoresponse-power relation.

Finally, the near-ideal power dependence of this structure is further demonstrated on a larger power range. A 532 nm laser source is employed to provide a large power density that LEDs cannot offer, while small difference to 535 nm LEDs in wavelength-dependent absorbance can be neglected. Figure 5h shows that the photoresponsivity of $WS_2/GaS_{0.87}$ heterostructure remains near 13 A/W in the range of a power density from ~0.01 to 232 mW/cm^2, while the photoresponsivity of monolayer WS_2 drops steeply from ~200 to <1 A/W in the same range (also see Fig. S14 for I−V curves). In other words, the heterostructure outperforms its individual components. Linear dynamic range (LDR) describes the range of linear response of photodetectors to the light intensity, which can be calculated by:

$$LDR = 10\log\left(\frac{P_{sat}R}{\sqrt{2eBI_{dark}}}\right)$$

where P_{sat} is the saturate light power when it deviates from linear response (which is larger than the light power at the density of 232 mW/cm^2), R_{532nm} is the photoresponsivity, B is the bandwidth (~0.1 Hz, see Fig. S12b). The obtained high LDR for the $WS_2/GaS_{0.87}$ heterostructure photodetector is larger than 73 dB, which surpasses many other 2D heterostructure photodetectors

and commercial photodetectors such as GaN (50 dB) and InGaAs (66 dB).[23, 26, 63-65] It should be noted that higher irradiance power might induce subtle damage to the WS_2 layer exposed to air, as monolayer WS_2 devices also exhibit weakened performance after that, therefore the measured LDR can be further improved with inert atmosphere protection. In Figure 5i, the figure of merits of photodetectors based on type-II heterostructures are summarized with photoresponsivity in x-axis and LDR in y-axis.[19, 21-23, 26, 29, 34, 66-71] While devices based on PVE show high LDR of 53−132 dB, the photoresponsivity value is less than 0.5 A/W. Other devices based on PGE or conventional sensitizers do not show linearity, and the photoresponsivity value often decay to under 10 A/W at high-power irradiance. In comparison, our work shows both high LDR value of 73 dB and high photoresponsivity value of 13 A/W. Further comparison of gain-bandwidth product with devices based on PVE is shown in Figure S15 for examine the gain-speed tradeoff. With its advantageous band structure, the simple bilayer $WS_2/GaS_{0.87}$ heterostructure proves that it can maintain a high photoresponsivity even at high-power irradiance and is promising for practical applications requiring wide linear working range such as in imaging systems.

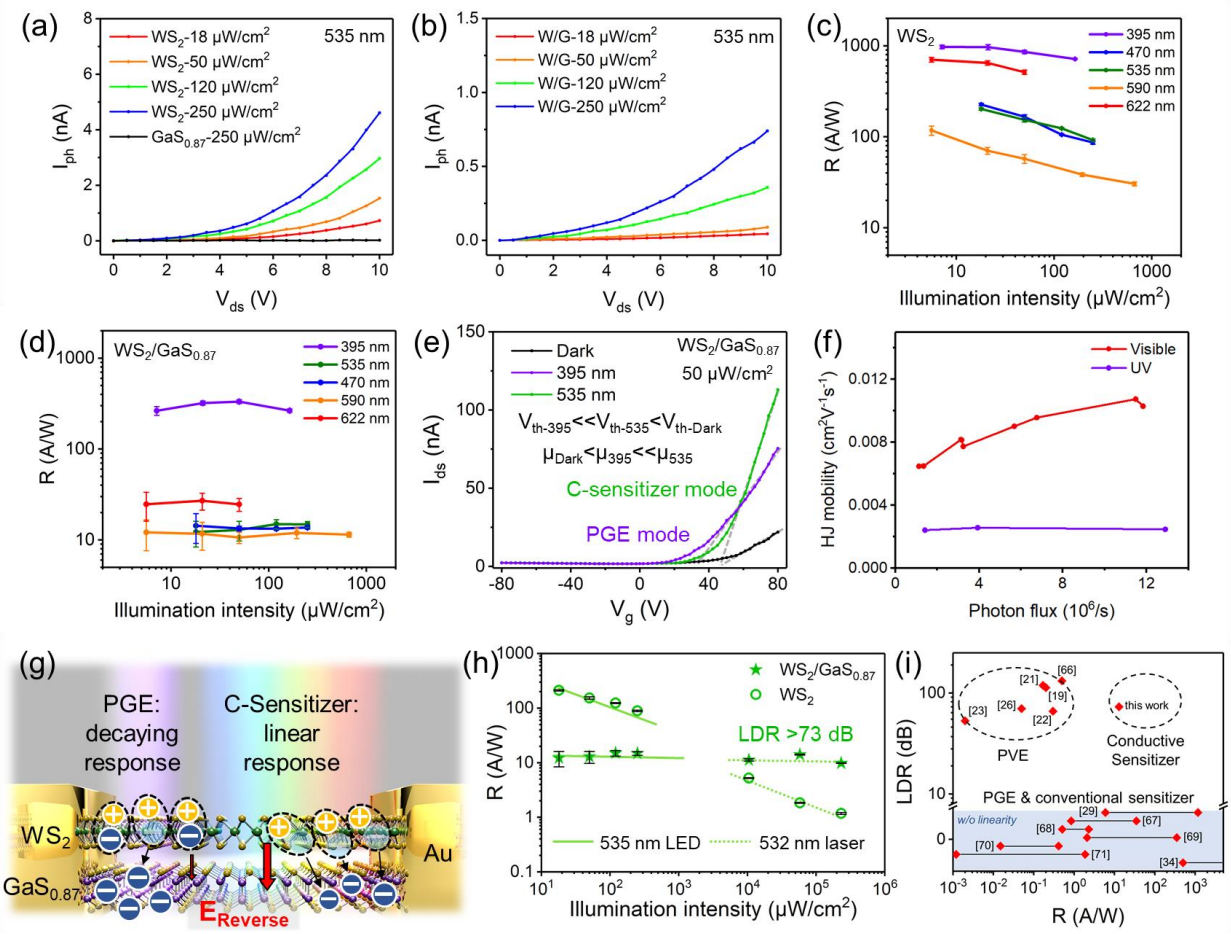

Figure 5. Optoelectronic properties of $WS_2/GaS_{0.87}$ heterostructure. (a) Photocurrent curve of WS_2 and $GaS_{0.87}$ FET devices under 535 nm illumination. (b) Photocurrent curve of $WS_2/GaS_{0.87}$ heterostructure FET device under 535 nm illumination. (c) Photoresponsivity of WS_2 photodetectors under different illumination intensity and wavelength. (d) Photoresponsivity of $WS_2/GaS_{0.87}$ photodetectors under different illumination intensity and wavelength. (e) Comparison of I−V_g curve of $WS_2/GaS_{0.87}$ heterostructure under dark and illumination (V_{ds}=2V). Under UV light (PGE mode) the transistor shows major change in threshold voltage, while under visible light (Conductive-sensitizer mode) it mainly shows change in transconductance and mobility. (f) Heterojunction mobility value *versus* photon flux under UV or visible illumination. (g) Schematic of carrier transfer and formation of reverse electric field in $WS_2/GaS_{0.87}$ heterostructure under visible light (Conductive-sensitizer mode) and UV light (PGE mode) photodetection. (h) Photoresponsivity of WS_2 and $WS_2/GaS_{0.87}$ photodetectors under 535 nm LED and 532 nm laser light source. (i) Comparison

of response sensitivity and linearity of photodetectors based on type-II 2D or 2D hybrid heterostructures from previous reports.

Conclusions

In this study, a conductive sensitizer strategy is proposed for achieving both high photoresponsivity and small photoresponsivity decay under high illumination power and is demonstrated thoroughly on bilayer $WS_2/GaS_{0.87}$ heterostructure with isotype type-II band alignment. A combination of spectroscopic techniques including XPS, CL and PL were used to show that intrinsic defects in the $GaS_{0.87}$ form a defect-induced band within the bandgap that alters the relative band offsets and consequently forms an isotype type-II heterojunction, resulting in efficient electron transfer from WS_2 to $GaS_{0.87}$. The defect-induced type-II heterojunction displays strong interlayer coupling and quenching behavior in the WS_2 PL. The transport characteristics of the bilayer $WS_2/GaS_{0.87}$ heterostructure deliver solid evidence of a $GaS_{0.87}$-dominated low-mobility carrier transport behavior under dark, and a transition to higher-mobility transport with increasing light illumination power. As a result, the photoresponsivity decay due to reduced carrier lifetime was compensated by the increase in heterostructure mobility, leading to a power dependence parameter value of nearly 1. Thanks to the bandgap values selection, the linear photoresponse-power relation is demonstrated across broad visible wavelength spectrum. A large linear dynamic range of 73 dB at a high photoresponsivity of 13 A/W is achieved for green light, with a large photogain between 480−1070, which is suitable for high performance photodetectors with a large working range. The excellent optoelectronic properties of this simple bilayer heterostructure can be further improved with enhancement in mobilities of both layers as well as contact engineering. These results provide insights into the important role of band and interface

modulation in offering heterostructures with outstanding properties and functions, and could be valuable in the future designing of more complex sets of heterojunctions to accomplish various tasks in next generation nano-electronic and -optoelectronics devices.

Experimental Methods

Fabrication of $WS_2/GaS_{0.87}$ heterojunctions:

Monolayer $GaS_{0.87}$ and WS_2 were synthesized according to our previously reported methods.[38-39] The WS_2 on SiO_2/Si substrates was then spin-coated with PMMA films, followed by etching in 1M KOH aqueous solutions for 3 hours before the WS_2 detached with the underlying substate. The PMMA films with WS_2 was washed with DI water for several times, then transferred onto the GaS film and put into vacuum for better adhesion. To better improve the interlayer interaction, the sample was further annealed at 120 °C for 30 min. Finally, acetone was used to remove the PMMA film. For the sulfur annealing process, 150 mg sulfur powder is loaded 6 cm upstream of the sample. The sulfur is heated first to 200 °C under 300 sccm Ar, and then the sample is heated to the same temperature and maintained for 30 min. A sulfur-rich atmosphere and low temperature is to avoid the 2D materials from degradation.

Characterizations:

XPS was characterized in a Thermo K-alpha XPS instrument with monochromatic Al Kα radiation (12 kV, 3 mA). Fitting and analysis of peak position and area was done in CasaXPS software. SEM characterization was conducted on Hitachi S-4300 at an accelerating voltage of 3.0 kV. CL spectrum was obtained in a JEOL JSM-6500F SEM with a Gatan MonoCL3 system under an accelerating voltage of 5 kV. AFM and KPFM analysis were done by Asylum Research MFP-3D

in AC mode with a silicon Tap300-G cantilever (BudgetSensors, spring constant ~40 N/m and resonant frequency ~300 kHz) and processed by Gwyddion software. Raman and PL characterization was performed in LabRam Aramis Raman spectrometer system with a 532 nm laser and a spot size of ~1 μm.

Device fabrication and measurements:

The gold electrodes were patterned directly on the heterostructure by JEOL 5500 FS EBL system using bilayer PMMA resist and developed in MIBK/IPA solution. After that, 80 nm Au was deposited by thermal evaporation, followed by lift-off in acetone. The source-drain current was measured using a Keithley 2400 source meter with two tungsten tips. For field-effect behavior studies, 300 nm SiO_2 layer was used as the dielectric layer and heavily *p*-doped Si was wired and connected to a Keithley 2400 source meter. In photocurrent studies, LEDs with varying wavelengths (Thorlabs, spot size ~300 μm) and 532 nm diode-pumped solid-state laser (Thorlabs, DJ532-40, spot size ~6 μm) were used as light sources. Power values of various light sources were recorded by a manually fixated power meter (Thorlab Optics PM100D, wavelength 200 nm–1000 nm) placed at the position of device. Measurements and observations were done on three devices for each type of devices which all showed consistent behavior ($GaS_{0.87}$; WS_2; $WS_2/GaS_{0.87}$). Owing to beginning of degradation of top WS_2 layer under large current in a humid and oxygen measuring environment, devices with the best and most robust performance were reported in Figure 4-5. All measurements were carried out under room temperature in ambient conditions.

Notes:

The authors declare no competing financial interest.

Acknowledgement:

We thank Y. Fan for helpful discussions.

Supporting Information Available: <SEM, Raman, PL and XPS characterizations; Schottky barrier height analysis; Absorption spectra; Response time; I−V and transfer curves under various illumination power>

TOC Graphic:

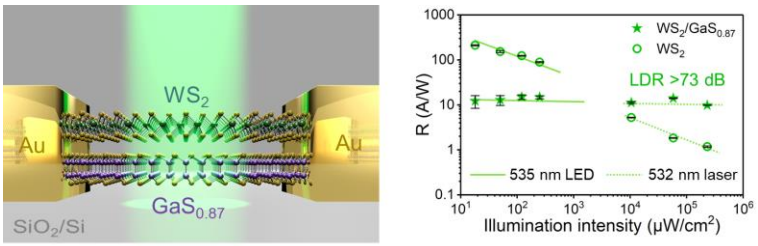

References:

1. Mueller, T.; Xia, F.; Avouris, P., Graphene Photodetectors for High-Speed Optical Communications. *Nature Photonics* **2010**, *4* (5), 297-301.

2. Koppens, F. H. L.; Mueller, T.; Avouris, P.; Ferrari, A. C.; Vitiello, M. S.; Polini, M., Photodetectors Based on Graphene, Other Two-Dimensional Materials and Hybrid Systems. *Nature Nanotechnology* **2014**, *9* (10), 780-793.

3. He, K.; Kumar, N.; Zhao, L.; Wang, Z.; Mak, K. F.; Zhao, H.; Shan, J., Tightly Bound Excitons in Monolayer WSe_2. *Physical Review Letters* **2014**, *113* (2), 026803.

4. Tsai, D.-S.; Liu, K.-K.; Lien, D.-H.; Tsai, M.-L.; Kang, C.-F.; Lin, C.-A.; Li, L.-J.; He, J.-H., Few-Layer MoS_2 with High Broadband Photogain and Fast Optical Switching for Use in Harsh Environments. *ACS Nano* **2013**, *7* (5), 3905-3911.

5. Tosun, M.; Fu, D.; Desai, S. B.; Ko, C.; Seuk Kang, J.; Lien, D.-H.; Najmzadeh, M.; Tongay, S.; Wu, J.; Javey, A., MoS_2 Heterojunctions by Thickness Modulation. *Scientific Reports* **2015**, *5* (1), 10990.

6. Huang, L.; Chen, Z. H.; Li, J. B., Effects of Strain on the Band Gap and Effective Mass in Two-Dimensional Monolayer GaX (X = S, Se, Te). *RSC Advances* **2015**, *5* (8), 5788-5794.

7. Chen, H.; Li, Y.; Huang, L.; Li, J. B., Intrinsic Defects in Gallium Sulfide Monolayer: A First-Principles Study. *RSC Advances* **2015**, *5* (63), 50883-50889.

8. Novoselov, K. S.; Mishchenko, A.; Carvalho, A.; Neto, A. H. C., 2D Materials and van der Waals Heterostructures. *Science* **2016**, *353* (6298), aac9439.

9. Frisenda, R.; Molina-Mendoza, A. J.; Mueller, T.; Castellanos-Gomez, A.; van der Zant, H. S. J., Atomically Thin *p-n* Junctions Based on Two-Dimensional Materials. *Chemical Society Reviews* **2018**, *47* (9), 3339-3358.

10. Kang, K.; Xie, S. E.; Huang, L. J.; Han, Y. M.; Huang, P. Y.; Mak, K. F.; Kim, C. J.; Muller, D.; Park, J., High-Mobility Three-Atom-Thick Semiconducting Films with Wafer-Scale Homogeneity. *Nature* **2015**, *520* (7549), 656-660.

11. Zhou, X.; Hu, X. Z.; Yu, J.; Liu, S. Y.; Shu, Z. W.; Zhang, Q.; Li, H. Q.; Ma, Y.; Xu, H.; Zhai, T. Y., 2D Layered Material-Based van der Waals Heterostructures for Optoelectronics. *Advanced Functional Materials* **2018**, *28* (14), 1706587.

12. Zhang, W. J.; Wang, Q. X.; Chen, Y.; Wang, Z.; Wee, A. T. S., van der Waals Stacked 2D Layered Materials for Optoelectronics. *2D Materials* **2016**, *3* (2), 022001.

13. Hong, X.; Kim, J.; Shi, S.-F.; Zhang, Y.; Jin, C.; Sun, Y.; Tongay, S.; Wu, J.; Zhang, Y.; Wang, F., Ultrafast Charge Transfer in Atomically Thin MoS_2/WS_2 Heterostructures. *Nature Nanotechnology* **2014**, *9* (9), 682-686.

14. Tran, K.; Moody, G.; Wu, F.; Lu, X.; Choi, J.; Kim, K.; Rai, A.; Sanchez, D. A.; Quan, J.; Singh, A.; Embley, J.; Zepeda, A.; Campbell, M.; Autry, T.; Taniguchi, T.; Watanabe, K.; Lu, N.; Banerjee, S. K.; Silverman, K. L.; Kim, S. *et al*., Evidence for Moiré Excitons in van der Waals Heterostructures. *Nature* **2019**, *567* (7746), 71-75.

15. Seyler, K. L.; Rivera, P.; Yu, H.; Wilson, N. P.; Ray, E. L.; Mandrus, D. G.; Yan, J.; Yao, W.; Xu, X., Signatures of Moiré-Trapped Valley Excitons in $MoSe_2$/WSe_2 Heterobilayers. *Nature* **2019**, *567* (7746), 66-70.

16. Kozawa, D.; Carvalho, A.; Verzhbitskiy, I.; Giustiniano, F.; Miyauchi, Y.; Mouri, S.; Castro Neto, A. H.; Matsuda, K.; Eda, G., Evidence for Fast Interlayer Energy Transfer in $MoSe_2$/WS_2 Heterostructures. *Nano Letters* **2016**, *16* (7), 4087-4093.

17. Li, L.; Ye, S.; Qu, J.; Zhou, F.; Song, J.; Shen, G., Recent Advances in Perovskite Photodetectors for Image Sensing. *Small* **2021,** *17* (18), 2005606.

18. García de Arquer, F. P.; Armin, A.; Meredith, P.; Sargent, E. H., Solution-Processed Semiconductors for Next-Generation Photodetectors. *Nature Reviews Materials* **2017,** *2* (3), 16100.

19. Ahn, J.; Kang, J. H.; Park, M. C.; Hwang, D. K., All 2D WSe_2/MoS_2 Heterojunction Photodiode and Its Image Sensor Application. *Optics Letters* **2020,** *45* (16), 4531-4534.

20. Buscema, M.; Island, J. O.; Groenendijk, D. J.; Blanter, S. I.; Steele, G. A.; van der Zant, H. S. J.; Castellanos-Gomez, A., Photocurrent Generation with Two-Dimensional van der Waals Semiconductors. *Chemical Society Reviews* **2015,** *44* (11), 3691-3718.

21. Lee, H. S.; Ahn, J.; Shim, W.; Im, S.; Hwang, D. K., 2D WSe_2/MoS_2 van der Waals Heterojunction Photodiode for Visible-Near Infrared Broadband Detection. *Applied Physics Letters* **2018,** *113* (16), 163102.

22. Wu, F.; Li, Q.; Wang, P.; Xia, H.; Wang, Z.; Wang, Y.; Luo, M.; Chen, L.; Chen, F.; Miao, J.; Chen, X.; Lu, W.; Shan, C.; Pan, A.; Wu, X.; Ren, W.; Jariwala, D.; Hu, W., High Efficiency and Fast van der Waals Hetero-Photodiodes with a Unilateral Depletion Region. *Nature Communications* **2019,** *10* (1), 4663.

23. Lee, C.-H.; Lee, G.-H.; van der Zande, A. M.; Chen, W.; Li, Y.; Han, M.; Cui, X.; Arefe, G.; Nuckolls, C.; Heinz, T. F.; Guo, J.; Hone, J.; Kim, P., Atomically Thin p–n Junctions with van der Waals Heterointerfaces. *Nature Nanotechnology* **2014**, *9* (9), 676-681.

24. Deng, Y.; Luo, Z.; Conrad, N. J.; Liu, H.; Gong, Y.; Najmaei, S.; Ajayan, P. M.; Lou, J.; Xu, X.; Ye, P. D., Black Phosphorus–Monolayer MoS_2 van der Waals Heterojunction p–n Diode. *ACS Nano* **2014**, *8* (8), 8292-8299.

25. Li, X. F.; Lin, M. W.; Lin, J. H.; Huang, B.; Puretzky, A. A.; Ma, C.; Wang, K.; Zhou, W.; Pantelides, S. T.; Chi, M. F.; Kravchenko, I.; Fowlkes, J.; Rouleau, C. M.; Geohegan, D. B.; Xiao, K., Two-Dimensional GaSe/$MoSe_2$ Misfit Bilayer Heterojunctions by van der Waals Epitaxy. *Science Advances* **2016**, *2* (4), e1501882.

26. Islam, A.; Lee, J.; Feng, P. X. L., Atomic Layer GaSe/MoS_2 van der Waals Heterostructure Photodiodes with Low Noise and Large Dynamic Range. *ACS Photonics* **2018**, *5* (7), 2693-2700.

27. Fang, H.; Hu, W., Photogating in Low Dimensional Photodetectors. *Advanced Science* **2017**, *4* (12), 1700323.

28. Zhang, W.; Chuu, C.-P.; Huang, J.-K.; Chen, C.-H.; Tsai, M.-L.; Chang, Y.-H.; Liang, C.-T.; Chen, Y.-Z.; Chueh, Y.-L.; He, J.-H.; Chou, M.-Y.; Li, L.-J., Ultrahigh-Gain Photodetectors Based on Atomically Thin Graphene-MoS_2 Heterostructures. *Scientific Reports* **2014**, *4* (1), 3826.

29. Tan, H.; Xu, W.; Sheng, Y.; Lau, C. S.; Fan, Y.; Chen, Q.; Tweedie, M.; Wang, X.; Zhou, Y.; Warner, J. H., Lateral Graphene-Contacted Vertically Stacked WS_2/MoS_2 Hybrid Photodetectors with Large Gain. *Advanced Materials* **2017**, *29* (46), 1702917.

30. Yang, T. F.; Zheng, B. Y.; Wang, Z.; Xu, T.; Pan, C.; Zou, J.; Zhang, X. H.; Qi, Z. Y.; Liu, H. J.; Feng, Y. X.; Hu, W. D.; Miao, F.; Sun, L. T.; Duan, X. F.; Pan, A. L., Van der Waals Epitaxial Growth and Optoelectronics of Large-Scale WSe_2/SnS_2 Vertical Bilayer *p-n* Junctions. *Nature Communications* **2017**, 8, 1906.

31. Ye, L.; Li, H.; Chen, Z.; Xu, J., Near-Infrared Photodetector Based on MoS_2/Black Phosphorus Heterojunction. *ACS Photonics* **2016**, *3* (4), 692-699.

32. Wang, J.; Han, J.; Chen, X.; Wang, X., Design Strategies for Two-Dimensional Material Photodetectors to Enhance Device Performance. *InfoMat* **2019,** *1* (1), 33-53.

33. Kufer, D.; Konstantatos, G., Photo-FETs: Phototransistors Enabled by 2D and 0D Nanomaterials. *ACS Photonics* **2016,** *3* (12), 2197-2210.

34. Kufer, D.; Nikitskiy, I.; Lasanta, T.; Navickaite, G.; Koppens, F. H. L.; Konstantatos, G., Hybrid 2D–0D MoS_2–PbS Quantum Dot Photodetectors. *Advanced Materials* **2015,** *27* (1), 176-180.

35. Jung, C. S.; Shojaei, F.; Park, K.; Oh, J. Y.; Im, H. S.; Jang, D. M.; Park, J.; Kang, H. S., Red-to-Ultraviolet Emission Tuning of Two-Dimensional Gallium Sulfide/Selenide. *ACS Nano* **2015**, *9* (10), 9585-9593.

36. Wang, X.; Sheng, Y.; Chang, R.-J.; Lee, J. K.; Zhou, Y.; Li, S.; Chen, T.; Huang, H.; Porter, B. F.; Bhaskaran, H.; Warner, J. H., Chemical Vapor Deposition Growth of Two-Dimensional Monolayer Gallium Sulfide Crystals Using Hydrogen Reduction of Ga_2S_3. *ACS Omega* **2018**, *3* (7), 7897-7903.

37. Luxa, J.; Wang, Y.; Sofer, Z.; Pumera, M., Layered Post-Transition-Metal Dichalcogenides (X−M−M−X) and Their Properties. *Chemistry – A European Journal* **2016**, *22* (52), 18810-18816.

38. Lu, Y.; Chen, J.; Chen, T.; Shu, Y.; Chang, R. J.; Sheng, Y.; Shautsova, V.; Mkhize, N.; Holdway, P.; Bhaskaran, H.; Warner, J. H., Controlling Defects in Continuous 2D GaS Films for High-Performance Wavelength-Tunable UV-Discriminating Photodetectors. *Advanced Materials* **2020**, *32* (7), e1906958.

39. Sheng, Y.; Chen, T.; Lu, Y.; Chang, R. J.; Sinha, S.; Warner, J. H., High-Performance WS_2 Monolayer Light-Emitting Tunneling Devices Using 2D Materials Grown by Chemical Vapor Deposition. *ACS Nano* **2019**, *13* (4), 4530-4537.

40. Cai, Z.; Liu, B.; Zou, X.; Cheng, H.-M., Chemical Vapor Deposition Growth and Applications of Two-Dimensional Materials and Their Heterostructures. *Chemical Reviews* **2018,** *118* (13), 6091-6133.

41. Lan, C.; Li, C.; Yin, Y.; Liu, Y., Large-Area Synthesis of Monolayer WS_2 and Its Ambient-Sensitive Photo-Detecting Performance. *Nanoscale* **2015**, *7* (14), 5974-5980.

42. Late, D. J.; Liu, B.; Matte, H.; Rao, C. N. R.; Dravid, V. P., Rapid Characterization of Ultrathin Layers of Chalcogenides on SiO_2/Si Substrates. *Advanced Functional Materials* **2012**, *22* (9), 1894-1905.

43. Aretouli, K. E.; Tsoutsou, D.; Tsipas, P.; Marquez-Velasco, J.; Aminalragia Giamini, S.; Kelaidis, N.; Psycharis, V.; Dimoulas, A., Epitaxial 2D $SnSe_2$/ 2D WSe_2 van der Waals Heterostructures. *ACS Applied Materials & Interfaces* **2016**, *8* (35), 23222-23229.

44. He, Z.; Wang, X.; Xu, W.; Zhou, Y.; Sheng, Y.; Rong, Y.; Smith, J. M.; Warner, J. H., Revealing Defect-State Photoluminescence in Monolayer WS_2 by Cryogenic Laser Processing. *ACS Nano* **2016,** *10* (6), 5847-5855.

45. Chow, P. K.; Jacobs-Gedrim, R. B.; Gao, J.; Lu, T.-M.; Yu, B.; Terrones, H.; Koratkar, N., Defect-Induced Photoluminescence in Monolayer Semiconducting Transition Metal Dichalcogenides. *ACS Nano* **2015**, *9* (2), 1520-1527.

46. Conley, H. J.; Wang, B.; Ziegler, J. I.; Haglund, R. F.; Pantelides, S. T.; Bolotin, K. I., Bandgap Engineering of Strained Monolayer and Bilayer MoS_2. *Nano Letters* **2013**, *13* (8), 3626-3630.

47. Tongay, S.; Zhou, J.; Ataca, C.; Liu, J.; Kang, J. S.; Matthews, T. S.; You, L.; Li, J.; Grossman, J. C.; Wu, J., Broad-Range Modulation of Light Emission in Two-Dimensional Semiconductors by Molecular Physisorption Gating. *Nano Letters* **2013**, *13* (6), 2831-2836.

48. Chernikov, A.; van der Zande, A. M.; Hill, H. M.; Rigosi, A. F.; Velauthapillai, A.; Hone, J.; Heinz, T. F., Electrical Tuning of Exciton Binding Energies in Monolayer WS_2. *Physical Review Letters* **2015**, *115* (12), 126802.

49. Wang, Y.; Zhang, S.; Di, H.; Cheng, J.; Li, Y.; Wu, S., Screening Effect of Graphite and Bilayer Graphene on Excitons in $MoSe_2$ Monolayer. *2D Materials* **2016**, *4* (1), 015021.

50. Peimyoo, N.; Yang, W.; Shang, J.; Shen, X.; Wang, Y.; Yu, T., Chemically Driven Tunable Light Emission of Charged and Neutral Excitons in Monolayer WS_2. *ACS Nano* **2014**, *8* (11), 11320-11329.

51. Wang, Y.; Cong, C.; Yang, W.; Shang, J.; Peimyoo, N.; Chen, Y.; Kang, J.; Wang, J.; Huang, W.; Yu, T., Strain-Induced Direct–Indirect Bandgap Transition and Phonon Modulation in Monolayer WS_2. *Nano Research* **2015**, *8* (8), 2562-2572.

52. Ding, L.; Ukhtary, M. S.; Chubarov, M.; Choudhury, T. H.; Zhang, F.; Yang, R.; Zhang, A.; Fan, J. A.; Terrones, M.; Redwing, J. M.; Yang, T.; Li, M.; Saito, R.; Huang, S., Understanding Interlayer Coupling in TMD-hBN Heterostructure by Raman Spectroscopy. *IEEE Transactions on Electron Devices* **2018,** *65* (10), 4059-4067.

53. Cong, C.; Shang, J.; Wang, Y.; Yu, T., Optical Properties of 2D Semiconductor WS_2. *Advanced Optical Materials* **2018**, *6* (1), 1700767.

54. Prasai, D.; Klots, A. R.; Newaz, A. K. M.; Niezgoda, J. S.; Orfield, N. J.; Escobar, C. A.; Wynn, A.; Efimov, A.; Jennings, G. K.; Rosenthal, S. J.; Bolotin, K. I., Electrical Control of Near-Field Energy Transfer between Quantum Dots and Two-Dimensional Semiconductors. *Nano Letters* **2015,** *15* (7), 4374-4380.

55. Kumar, R.; Verzhbitskiy, I.; Giustiniano, F.; Sidiropoulos, T. P. H.; Oulton, R. F.; Eda, G., Interlayer Screening Effects in WS_2/WSe_2 van der Waals Hetero-Bilayer. *2D Materials* **2018**, *5* (4), 041003.

56. Zhu, B.; Chen, X.; Cui, X., Exciton Binding Energy of Monolayer WS_2. *Scientific Reports* **2015**, *5* (1), 9218.

57. Mouri, S.; Miyauchi, Y.; Toh, M.; Zhao, W.; Eda, G.; Matsuda, K., Nonlinear Photoluminescence in Atomically Thin Layered WSe_2 Arising from Diffusion-Assisted Exciton-Exciton Annihilation. *Physical Review B* **2014,** *90* (15), 155449.

58. Lee, Y.-H.; Yu, L.; Wang, H.; Fang, W.; Ling, X.; Shi, Y.; Lin, C.-T.; Huang, J.-K.; Chang, M.-T.; Chang, C.-S.; Dresselhaus, M.; Palacios, T.; Li, L.-J.; Kong, J., Synthesis and Transfer of Single-Layer Transition Metal Disulfides on Diverse Surfaces. *Nano Letters* **2013**, *13* (4), 1852-1857.

59. Schulman, D. S.; Arnold, A. J.; Das, S., Contact Engineering for 2D Materials and Devices. *Chemical Society Reviews* **2018,** *47* (9), 3037-3058.

60. Fan, Y.; Zhou, Y.; Wang, X.; Tan, H.; Rong, Y.; Warner, J. H., Photoinduced Schottky Barrier Lowering in 2D Monolayer WS_2 Photodetectors. *Advanced Optical Materials* **2016**, *4* (10), 1573-1581.

61. Pak, J.; Min, M.; Cho, K.; Lien, D.-H.; Ahn, G. H.; Jang, J.; Yoo, D.; Chung, S.; Javey, A.; Lee, T., Improved Photoswitching Response Times of MoS_2 Field-Effect Transistors by Stacking *p*-Type Copper Phthalocyanine Layer. *Applied Physics Letters* **2016,** *109* (18), 183502.

62. Mitta, S. B.; Choi, M. S.; Nipane, A.; Ali, F.; Kim, C.; Teherani, J. T.; Hone, J.; Yoo, W. J., Electrical Characterization of 2D Materials-Based Field-Effect Transistors. *2D Materials* **2020,** *8* (1), 012002.

63. Roy, K.; Ahmed, T.; Dubey, H.; Sai, T. P.; Kashid, R.; Maliakal, S.; Hsieh, K.; Shamim, S.; Ghosh, A., Number-Resolved Single-Photon Detection with Ultralow Noise van der Waals Hybrid. *Advanced Materials* **2018**, *30* (2), 1704412.

64. Khan, M. A.; Kuznia, J. N.; Olson, D. T.; Hove, J. M. V.; Blasingame, M.; Reitz, L. F., High - Responsivity Photoconductive Ultraviolet Sensors Based on Insulating Single-Crystal GaN Epilayers. *Applied Physics Letters* **1992**, *60* (23), 2917-2919.

65. Gong, X.; Tong, M.; Xia, Y.; Cai, W.; Moon, J. S.; Cao, Y.; Yu, G.; Shieh, C.-L.; Nilsson, B.; Heeger, A. J., High-Detectivity Polymer Photodetectors with Spectral Response from 300 nm to 1450 nm. *Science* **2009**, *325* (5948), 1665-1667.

66. Ahn, J.; Kang, J. H.; Kyhm, J.; Choi, H. T.; Kim, M.; Ahn, D. H.; Kim, D. Y.; Ahn, I. H.; Park, J. B.; Park, S.; Yi, Y.; Song, J. D.; Park, M. C.; Im, S.; Hwang, D. K., Self-Powered Visible-Invisible Multiband Detection and Imaging Achieved Using High-Performance 2D $MoTe_2/MoS_2$ Semivertical Heterojunction Photodiodes. *ACS Applied Materials & Interfaces* **2020,** *12* (9), 10858-10866.

67. Luo, P.; Zhuge, F.; Wang, F.; Lian, L.; Liu, K.; Zhang, J.; Zhai, T., PbSe Quantum Dots Sensitized High-Mobility Bi_2O_2Se Nanosheets for High-Performance and Broadband Photodetection beyond 2 μm. *ACS Nano* **2019,** *13* (8), 9028-9037.

68. Xue, Y.; Zhang, Y.; Liu, Y.; Liu, H.; Song, J.; Sophia, J.; Liu, J.; Xu, Z.; Xu, Q.; Wang, Z.; Zheng, J.; Liu, Y.; Li, S.; Bao, Q., Scalable Production of a Few-Layer MoS_2/WS_2 Vertical Heterojunction Array and Its Application for Photodetectors. *ACS Nano* **2016,** *10* (1), 573-580.

69. Yang, Y.; Huo, N.; Li, J., Gate Modulated and Enhanced Optoelectronic Performance of $MoSe_2$ and CVD-Grown MoS_2 Heterojunctions. *RSC Advances* **2017,** *7* (65), 41052-41056.

70. Yang, T.; Li, X.; Wang, L.; Liu, Y.; Chen, K.; Yang, X.; Liao, L.; Dong, L.; Shan, C.-X., Broadband Photodetection of 2D Bi_2O_2Se–$MoSe_2$ Heterostructure. *Journal of Materials Science* **2019,** *54* (24), 14742-14751.

71. Sar, H.; Taghipour, N.; Lisheshar, I. W.; Delikanli, S.; Demirtas, M.; Demir, H. V.; Ay, F.; Perkgoz, N. K., MoS_2 Phototransistor Sensitized by Colloidal Semiconductor Quantum Wells. *Advanced Optical Materials* **2020,** *8* (24), 2001198.